Article

Photo-ferroelectric perovskite interfaces for boosting V_{OC} in efficient perovskite solar cells

Giovanni Pica[1], Lorenzo Pancini[1], Christopher E. Petoukhoff [2], Badri Vishal[2], Francesco Toniolo[1], Changzeng Ding [3], Young-Kwang Jung[4,5], Mirko Prato [6], Nada Mrkyvkova [7], Peter Siffalovic [7], Stefaan De Wolf [2], Chang-Qi Ma [3], Frédéric Laquai [2], Aron Walsh [4,8] & Giulia Grancini [1] ✉

Interface engineering is the core of device optimization, and this is particularly true for perovskite photovoltaics (PVs). The steady improvement in their performance has been largely driven by careful manipulation of interface chemistry to reduce unwanted recombination. Despite that, PVs devices still suffer from unavoidable open circuit voltage (V_{OC}) losses. Here, we propose a different approach by creating a photo-ferroelectric perovskite interface. By engineering an ultrathin ferroelectric two-dimensional perovskite (2D) which sandwiches a perovskite bulk, we exploit the electric field generated by external polarization in the 2D layer to enhance charge separation and minimize interfacial recombination. As a result, we observe a net gain in the device V_{OC} reaching 1.21 V, the highest value reported to date for highly efficient perovskite PVs, leading to a champion efficiency of 24%. Modeling depicts a coherent matching of the crystal and electronic structure at the interface, robust to defect states and molecular reorientation. The interface physics is finely tuned by the photoferroelectric field, representing a new tool for advanced perovskite device design.

The continuous advancements in perovskite PVs place this technology at the forefront of the modern solar landscape, offering a concrete opportunity for commercialization[1–3]. Intense efforts have been mainly dedicated to interface chemical manipulation, spanning from the use of molecular additives to the deposition of conformal crystalline or amorphous layers, pivotal to increase device efficiency and stability[4–6]. Gradient interfaces are generally obtained either by compositional engineering, or by tuning perovskite phase, or dimensionality[7,8]. The latest, commonly known as 2D/3D approach, has become a standard strategy for boosting device performances by specifically addressing

open circuit voltage (V_{OC}) losses, reducing charge recombination[9,10]. Beyond that, no new physical phenomena have been exploited so far to tackle this issue. Given the necessity of charge separation, an interfacial electric field could serve as a potential solution. Ferroelectricity, which manifests when a spontaneous, permanent electrical polarization is activated by an external electric field, can modulate the interfacial electrical field distribution, with potential impact on device performances[11,12]. If such polarization is coupled with the ability of a photoactive semiconductor to convert light into electricity, it results in the formation of a photo-ferroelectric device[13–16]. Ferroelectricity in

[1]Department of Chemistry & INSTM, Università Degli Studi Di Pavia, Pavia, Italy. [2]Physical Sciences and Engineering Division (PSE), KAUST Solar Center (KSC), King Abdullah University of Science and Technology (KAUST), Thuwal, Kingdom of Saudi Arabia. [3]i-Lab & Printable Electronics Research Center, Suzhou Institute of Nano-Tech and Nano-Bionics (SINANO), Chinese Academy of Sciences (CAS), Suzhou, China. [4]Department of Materials, Imperial College London, London, UK. [5]Department of Chemical Engineering and Biotechnology, University of Cambridge, Cambridge, UK. [6]Istituto Italiano di Tecnologia (IIT), Materials Characterization Facility, Genova, Italy. [7]Center for Advanced Materials Application, Slovak Academy of Sciences, Bratislava, Slovakia. [8]Department of Physics, Ewha Womans University, Seoul, Korea. ✉e-mail: giulia.grancini@unipv.it

halide perovskites (HPs) – due to their soft nature and ionic composition- remains a subject of debate, despite theoretically modeled[17–23]. However, ferroelectricity can be imparted in 2D perovskites using large organic cations with a strong permanent dipole moment[15]. The implementation of 2D ferroelectric perovskites in devices is still in its early stages, primarily explored in photodetectors[16]. Recently, organic salts with large dipole moment have been incorporated as surface passivants, leading to the formation of a 2D perovskite capping layer, suggesting potential ferroelectric activity[24]. Additionally, fluorinated polymers have been used as dopants in the bulk of the perovskite active layer, responsible for an increase in the internal built in electric field[25].

Differently, we design a photo-ferroelectric 2D/3D/2D perovskite junction by integrating a 2D ferroelectric perovskite single crystals in the perovskite bulk, as a tool to manipulate the perovskite interfacial electric field. Upon external polarization, the 2D ferroelectric layer polarizes, generating an electric field that adds to the original built-in electric field. As a result, device performance improves, leading to a boost in the device V_{OC} to as high as 1.21 V - surpassing current records of high-efficiency PSCs – and achieving a power conversion efficiency (PCE) of 24%. Combined transient optical and THz measurements performed on both the film and the device, reveal that the presence of the photo-ferroelectric interface synergistically improves charge collection while reducing recombination by driving photogenerated electrons and holes further apart. This lowers non-radiative recombination, pushing the device closer to the Shockley-Queisser (S-Q) thermodynamic limit. Atomistic modeling confirms the beneficial effect of the resulting interfacial electric field. The 2D/3D interfaces do not produce any detrimental traps and molecular reorientation at the interface produces a strong interfacial dipole with a potential shift of ± 2 V, demonstrating the potential impact of molecular order on carrier dynamics.

Results

Design of a double photoferroelectric 2D/3D/2D perovskite interface

To design a perovskite junction composed of a 3D triple-cation perovskite bulk sandwiched between thin layers of ferroelectric 2D perovskite, we utilize established knowledge regarding the formation of gradient interfaces. When a 2D perovskite crystalline seed is added to the precursor solution of a bulk 3D perovskite, the 2D layer typically forms at the bottom of the 3D structure[26]. Additionally, it has been demonstrated that fluorinated low dimensional perovskites (LDP), due to their tendency to self-organize into highly stable and ordered assemblies, spontaneously assemble on the top surface of the 3D perovskite[27]. Therefore, to template the formation of a 2D/3D/2D junction we selected the (4,4-DFPD)$_2$PbI$_4$, (where 4,4-DFPD is 4,4-difluoropiperidinium) as fluorinated, ferroelectric 2D perovskite. First, we fabricated (4,4-DFPD)$_2$PbI$_4$ single crystals (owing to a polar space group Aba2), which are known to possess a ferroelectric character mainly ascribed to the order–disorder transition of the organic cation[28]. The (4,4-DFPD)$_2$PbI$_4$ single crystals were dissolved in a solution of DMF:DMSO (4:1) together with the Cs$_{0.05}$FA$_{0.79}$MA$_{0.16}$Pb(I$_{0.9}$Br$_{0.1}$)$_3$ (methylammonium -MA, formamidinium -FA) 3D precursors to obtain a 550 nm perovskite layer. Figure 1a shows time-of-flight secondary ion mass spectrometry (ToF-SIMS) analysis on the perovskite thin film deposited on indium tin oxide (ITO). Specifically, to verify the qualitative distribution of the 2D perovskite in cross section, i.e., across the sample thickness, we map the fluoride (F⁻) and - as a reference - the SnO⁻ signals. The ToF-SIMS reveals a clear presence of F⁻ species mainly located at the 3D perovskite interface with the ITO substrate along with a residual, but with a non- negligible content, at the top surface of 3D perovskite, indicating an uneven coverage. To visualize such elemental distribution, we also perform X-ray photoelectron spectroscopy (XPS) measurements. The results confirm the presence of F- at the top

surface of the 3D perovskite (Figs. S1, S2, S3 and Table S1), corroborating the previous results. To understand whether such element is present as a dispersion of the organic cation or as part of a 2D structure, we performed photoluminescence (PL) spectroscopy, exciting the sample from both front and back sides (Fig. 1b). Upon front-side excitation, the spectrum indicates a main peak at 780 nm – assigned to the 3D bulk emission - along with a weaker signature at shorter wavelength side, peaking at 525 nm, which is ascribed to the 2D emission (with $n = 1$ phase)[29]. Upon back/side excitation, both the features persist and closer inspection reveals two peaks at shorter wavelengths: 525 nm (as in the front) and 560 nm which are related to the emission from a combination of $n = 1$ and $n = 2$ 2D perovskite phases, respectively[29,30]. Such measurements univocally prove the presence of a 2D perovskite layers on both the top and bottom surfaces, sandwiching the 3D perovskite bulk and forming a 2D/3D/2D junction, as illustarted in the schematic in Fig. 1c. Transmission electron microscopy (TEM) images in Fig. 1d–f shows the cross-section structure of the sandwiched interface in a device configuration based on ITO/MeO-2PACz/perovskite/PCBM/Ag. The different layers composing the stack are clearly distinguishable: a -60 nm thick 2D ($n = 2$) layer is formed on the ITO, as confirmed by low-mag TEM and HAADF-STEM (Fig. 1d, e). On top of it, the 3D perovskite is evident and forming the bulk of the sandwich (Fig. 1d, f). Lastly, a - 30 nm 2D ($n = 1$) layer exhibits a discrete distribution at top surface (Fig. 1d–f). HR-TEM and corresponding fast Fourier transform (FFT) confirm the crystalline nature of bottom, bulk, and top perovskite phases (Fig. 1e, f). Grazing incident wide angle X-ray scattering (GIWAXS) investigations further support the vertical distribution of the 2D/3D/2D junction, in agreement with TEM analysis (see Supplementary note 6).

To create a polar interface using the ferroelectric (4,4-DFPD)$_2$PbI$_4$-based 2D, we first verify the polarization behavior of the sandwiched 2D/3D/2D interface using piezoresponse force microscopy (PFM) (Fig. 1g–j)[31]. The amplitude and phase of PFM vibrational signal depends on the intensity of the ferroelectric domains within the material and on their polarization direction, respectively. PFM maps are shown in Fig. 1g–j, showing: (g) the topography; (h) the PFM amplitude; (i-j) the phase at +3 V and −3 V, respectively. A close correlation between grain distribution and ferroelectric domains is evident when comparing Fig. 1g, h, as highlighted by the dashed areas on the maps. Furthermore, a defining feature of ferroelectric materials is the reversal of ferroelectric domain direction when the externally applied polarization field is switched. Such behavior is clearly observed in Fig. 1i, j, where the orientation of the ferroelectric domains reverses upon changing the sign of the applied external voltage. For a more quantitative analysis, we analyse the signal profiles across selected grain boundaries (indicated by white lines on the maps). Figure 1k shows the topography, PFM amplitude and PFM phase with +3 V polarization bias which perfectly match to each other. Conversely, when the polarization bias is reverted to −3V, the corresponding phase profiles shows an opposite trend, confirming the ferroelectric effect. Notably, such contrast is absent in the bare 3D sample ("control" in Fig. S4). PFM analysis on the bottom surface (see Fig. S5) show a threefold increase in PFM amplitude compared to the top 2D surface, indicating a thicker and more homogeneous distribution of the ferroelectric 2D perovskite at the bottom of the film. Overall, these measurements assess the formation of a double ferroelectric effect of the 2D at both top and bottom interfaces.

Real space model of ferroelectric 2D/3D interface

To provide insights into the underlying atomistic processes, we constructed a real space model of the 2D/3D interface (note that a full 2D/3D/2D is beyond the reach of available computational resources). The relaxed crystal structures of the end member compounds (4,4-DFPD)$_2$PbI$_4$ and FAPbI$_3$ were combined to form an interface oriented along [001] using averaged in-plane lattice constants. Relaxation of the
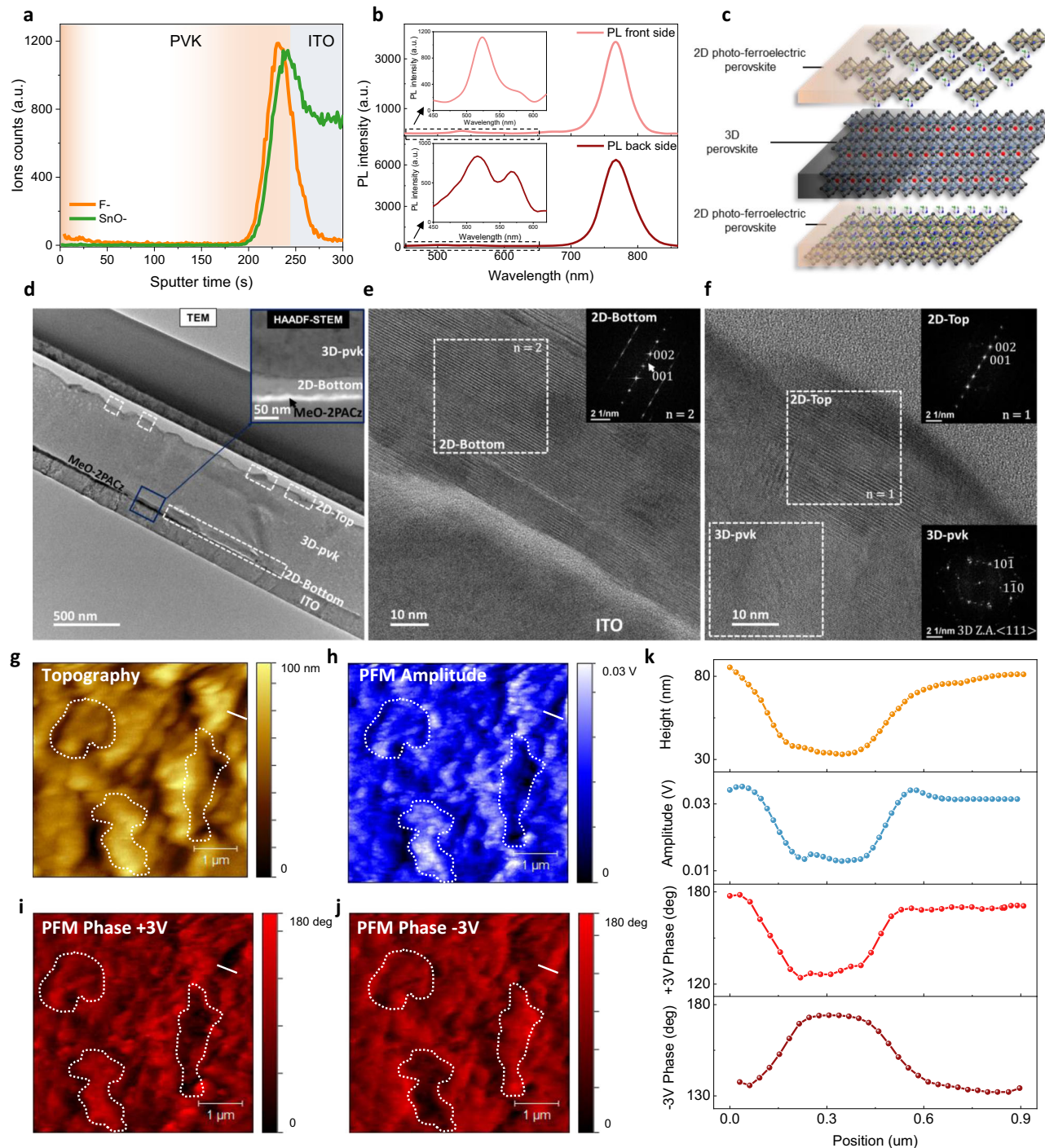
Fig. 1 | Design and evidence of a ferroelectric 2D/3D/2D perovskite hetero-structure. a Time of flight secondary ion mass spectrometry (ToF-SIMS) depth element profile and (**b**) photoluminescence (PL) spectrum of photo-ferroelectric perovskite thin film deposited on ITO. **c** Graphical representation of the 2D/3D/2D perovskite heterostructure. **d** Cross-sectional low mag transmission electron microscopy (TEM) image of device configuration with thick (~ 60 nm) dis-continuous horizontal 2D at bottom (Zoom-in HAADF-STEM (inset)), and thinner (~30 nm) more discrete at top. **e** HRTEM of 2D-Bottom is $n = 2$ confirm by FFT

(inset). **f** Similarly 2D-Top is $n = 1$ on top of 3D-pvk confirm by FFT (inset). **g** Topography, (**h**) amplitude, (**i, j**) phase and (**k**) corresponding profiles of a selected region of photo-ferroelectric perovskite thin film obtained from piezo-responce force microscopy (PFM) measurements. The phase signal is recorded with both a voltage bias of +3 V and −3 V to highlight that a switch in the orientation of the polar domains of the material is induced by changing the sign of the voltage bias applied to the tip.

separation along the c axis was performed to minimise strain in the 520 atom supercell. Initial analysis assumed an antiferroelectric ordering of the molecular cations (no z component in the spontaneous polariza-tion of the 2D layers). The charge density difference along the c axis, shown in Fig. 2a, confirms no significant charge transfer across the interface. However, internal redistribution of charge results in a local

potential difference of 0.04 V. The calculated valence band offset is 0.32 eV and the conduction band offset is 0.13 eV in a straddling con-figuration due to the wider band gap of the 2D. In contrast, molecular reorientation at the interface produces a strong interfacial dipole, causing a potential shift of ±2 V depending on the configurations (Fig. 2b–d). This is much greater in magnitude than the original band
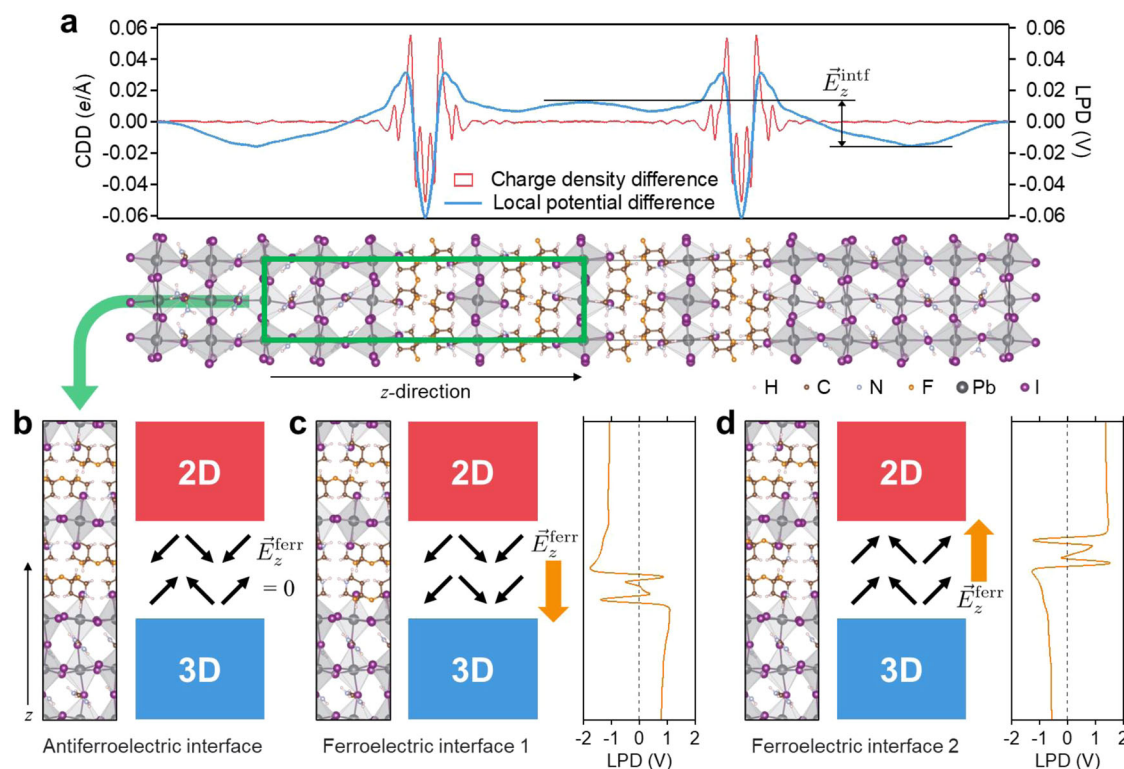
Fig. 2 | Real space model of the 2D/3D interface. a Calculated charge density difference (CDD) and local potential difference (LPD) across the entire superlattice of the (4,4-DFPD)$_2$PbI$_4$/FAPbI$_3$ interface, assuming an antiferroelectric configuration of 4,4-DFPD molecular cations. **b** Atomic geometry and schematic diagram illustrating the 2D/3D interface with an antiferroelectric molecular configuration, where the black arrows indicate the electric dipole directions of 4,4-DFPD and $\vec{E}_z^{ferr}$

represents the resulting electric field along the z direction. Atomic geometry and schematic diagrams for the 2D/3D interface in a ferroelectric configuration, with the net dipole along the z-direction towards the (**c**) 3D perovskite and (**d**) the 2D perovskite. The resultant potential difference between the 2D and 3D perovskites is depicted by the orange curves.

offset, highlighting the potential impact of molecular order on carrier dynamics.

Photovoltaic performances of the photoferroelectric 2D/3D/2D perovskite based solar cells

To assess the potential ferroelectric role of the 2D also at the bottom interface, we integrate the 2D/3D/2D sequence in a working solar cell, applying an external field to induce a net polarization in the ferroelectric 2D. Figure 3a–d displays the PV parameters for both the "control" and the 2D/3D/2D junction (denoted as "Photo-ferr") with and without a voltage bias of −0.3 V applied for 15 s prior to current-voltage scans (forward and reverse JV curves reported in Fig. S6). First, the inclusion of the 2D interfaces improved the device fill factor (FF) and V$_{OC}$, ultimately enhancing its PCE. Upon polarization, i.e., keeping the device under illumination at −0.3 V before the current-voltage (J-V) scan, the Photo-ferr device shows a remarkable improvement in all PV parameters compared to the biased control device, obtaining a maximum PCE of 24%, FF of 84% and a maximum V$_{OC}$ of 1.21 V (Fig. S7). No variation in morphology (Fig. S8), band-gap of the active material (Figs. S9 and S10), or band alignment (Fig. S11) - factors typically contributing to V$_{OC}$ improvement - are observed following the integration of the ferroelectric 2D. This suggests that the performance enhancement is inherently linked to the presence of a photo-ferroelectric interface, as schematically depicted in Fig. 3e. Upon external polarization, the dipoles in the 2D layer align, creating an additional electric field ($\vec{E}_{ferr}$) which constructively adds to the built-in electric field ($\vec{E}_{bi}$) responsible for the photogenerated current. This 2D-based photo-ferroelectric interface is key to boosting device performance. Notably, polarization leads to a reduction in statistical dispersion of all PV parameters of the 2D/3D/2D -based

device, as the dipoles are forced to align parallel to $\vec{E}_{bi}$, which may only partially align without the external field. The concept is further highlighted by the effect of a polarization bias on the current-voltage curves, reported in Fig. 3f. Upon polarization, the control device shows only a 3 mV increase in the V$_{OC}$ with respect to the unbiased one, which can be related to the commonly observed light soaking effect and ion motion[32]. In contrast, the photo-ferroelectric device exhibits a remarkable increase of 15 mV in the V$_{OC}$. Consequently, the champion photo-ferroelectric device delivers a V$_{OC}$ of 1.21 V, representing 92% and 97% of the theoretical Shockley-Queisser and radiative V$_{OC}$ limit, respectively, with only 44 mV of V$_{OC}$ losses (Fig. 3g, Figure S18 and Eq. S5). This value is a world record for perovskite solar cells with PCE > 22% reported to date, demonstrating the potential of our photo-ferroelectric interface. To further illustrate, Fig. 3h, i shows the PCE and the V$_{OC}$ values, respectively, retrieved from literature database for absorbers with band gaps between 1.5 eV and 1.7 eV[26]. Furthermore, we evaluated the long-term stability and the stabilized power and voltage output at MPP (Figs. S12 and S13). The photo-ferroelectric device retained more than 90% of its relative PCE after over 1000 h, while the control experienced a severe 40% PCE loss, further confirming the importance of our photo-ferroelectric interface in improving devices' stability. To strengthen our results and to generalize the validity of our method, we extended our approach from 1.59 to a 1.54 eV band gap triple cation perovskite, mantaining the same 2D ferroelectric interfaces in terms of material composition and processing. Results (see supplementary note 2) show that when the smaller band gap 3D perovskite is sandwiched within the ferroelectric 2Ds, polarization induces a clear improvement in the device Voc (Fig. S15), due to the formation of a double photo-ferroelectric junction.
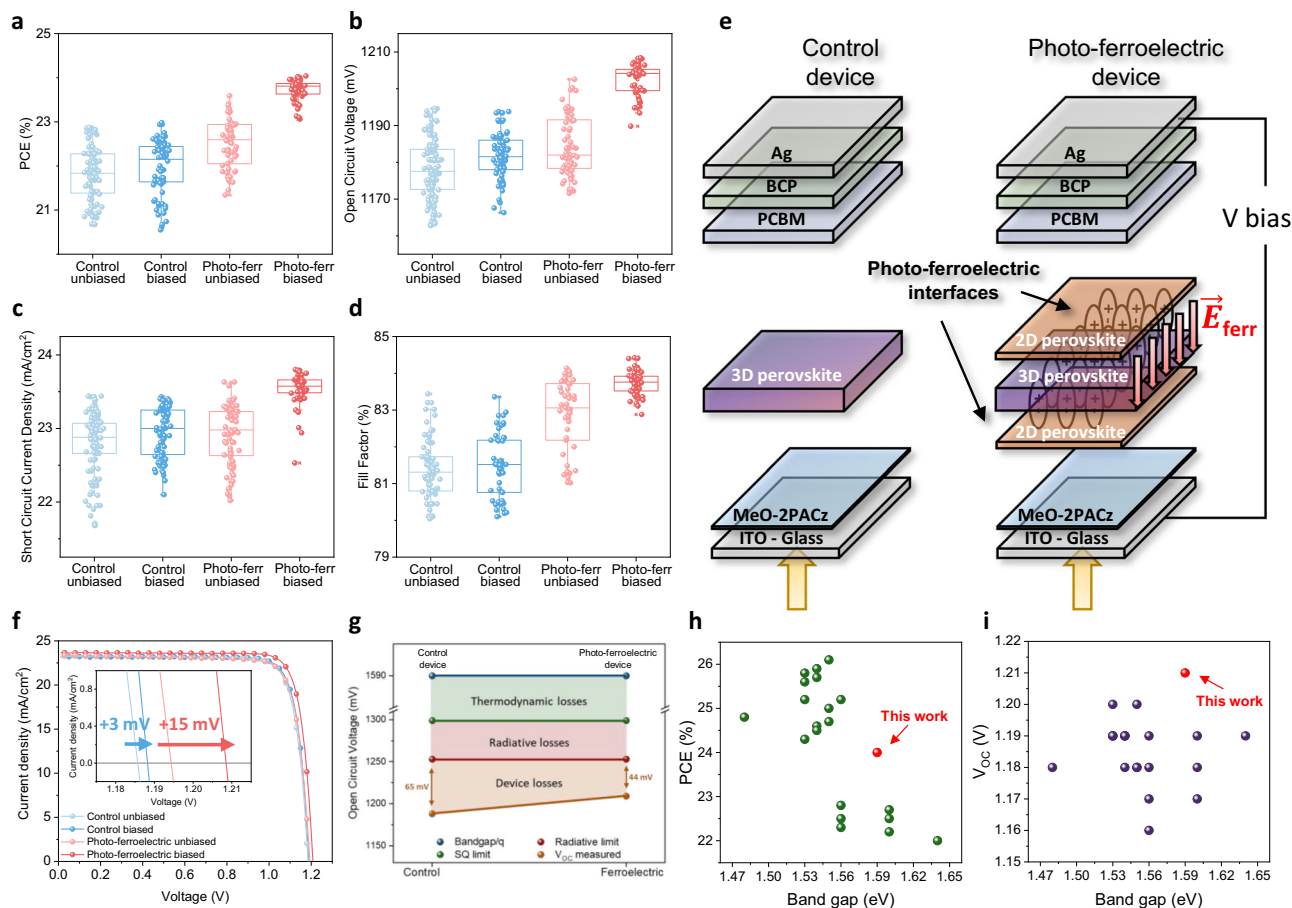
Fig. 3 | **Photovoltaic performances of the photoferroelectric 2D/3D/2D perovskite based solar cells.** Power conversion efficiency (PCE) (**a**), open circuit voltage (V_{OC}) (**b**), short circuit current density (J_{SC}) (**c**) and fill factor (FF) (**d**) for both control and photo-ferroelectric devices with and without an applied voltage bias to highlight the effect of domains reorientation on the photovoltaic parameters. Graphical representation of the effect of polarization bias on the photo-ferroelectric device, where $\vec{E}_{ferr}$ represents the additional electric field provided by the ferroelectric perovskite int**e**rfaces (**e**). Effect of voltage bias on the current-voltage (JV) curve (**f**) and detailed V_{OC} losses analysis for the control and photo-ferroelectric devices. **g** PCE (**h**) and Voc (**i**) literature values for PSCs between 1.47 eV and 1.65 eV, with PCE > 22% and V_{OC} > 1.16 V.

Steady-state and time-resolved electro-optical analysis

To elucidate the mechanisms behind the performance enhancement induced by the photo-ferroelectric interface, we performed a combined steady state and transient spectroscopic analysis using time-resolved terahertz (THz) spectroscopy, femtosecond transient absorption (TA), time-resolved photoluminescence (TRPL) spectroscopy, and photoluminescence mapping. Specifically, to disentangle the underlying processes at each interface, the systems chosen for in-depth investigation consisted of neat perovskite thin films deposited on quartz glass substrates ("Control" and "Photo-ferr"), stacks of quartz/MeO-2PACz/perovskite ("MeO/Control" and "MeO/Photo-ferr"), and complete device-like stacks ("MeO/Control/PCBM" and "MeO/Photo-ferr/PCBM"). Figure 4a, d shows the THz signal decays of the control and photo-ferroelectric samples, respectively, following 470 nm pulsed photoexcitation. The decay dynamics were fitted using bi-exponential functions, with the results summarized in Table 1. For the control (Fig. 4a), the shorter lifetime component (τ_1, Table 1) remains unchanged upon addition of the transport layers, while a statistically significant (see also Figs. S16 and S17) decrease in the longer lifetime component (τ_2, Table 1) was observed when changing from the neat film to the half and full device. An opposite trend was observed for the photo-ferroelectric interface (Fig. 4d): here, τ_1 showed a statistically significant (Figs. S16 and S17) decrease in the device configuration, while τ_2 remains unaffected. These observations can be rationalized by considering the following: i) the overall THz signal decay of the neat

photo-ferroelectric interface is longer than that of the control (Fig. S16a, b), indicating reduced non-radiative recombination[33–35] due to the intrinsic polarization field, which separates the photogenerated charge carriers (as further confirmed by PL, TRPL, and transient photovoltage measurements in Figs. S18, S19 and S20, respectively); (ii) considering that the THz signal, measured as the differential transmission signal ($\frac{\Delta T}{T}$) is proportional to the product of the time-dependent charge carrier density $n(t)$ and charge carrier mobility $\mu(t)$, i.e., $\frac{\Delta T}{T} \alpha \, \sigma(t) \alpha \, n(t)\mu(t)$, the reduction of τ_1 in the photo-ferroelectric interface can be ascribed to either a reduction of $n(t)$ (which in turn can be related to recombination or eventual charge transfer with the charge extracting layers[33,35,36]), a decrease in $\mu(t)$ or both. To disentangle the aforementioned mechanisms, we performed TA measurements using the same excitation conditions on the same stacks analysed with THz spectroscopy. Figure 4b, e shows the dynamics at 780 nm, corresponding to the peak of the photobleaching (PB) signal. Since $\frac{\Delta T}{T} \alpha \, n(t)$, its decay reflects the evolution of the charge carrier density. Using the same bi-exponential parametrization of the TA data as performed on the THz data, the same trend was observed: τ_2 was reduced for the "control" (Fig. 4b and Table 1) upon addition of the transport layers but remained unaltered for the photo-ferroelectric interface. Meanwhile, the opposite effect was confirmed for τ_1, which remained constant upon addition of the transport layers for the control but decreased for the photo-ferroelectric samples. Overall, the TA analysis supports a reduction in carrier density, consistent with the
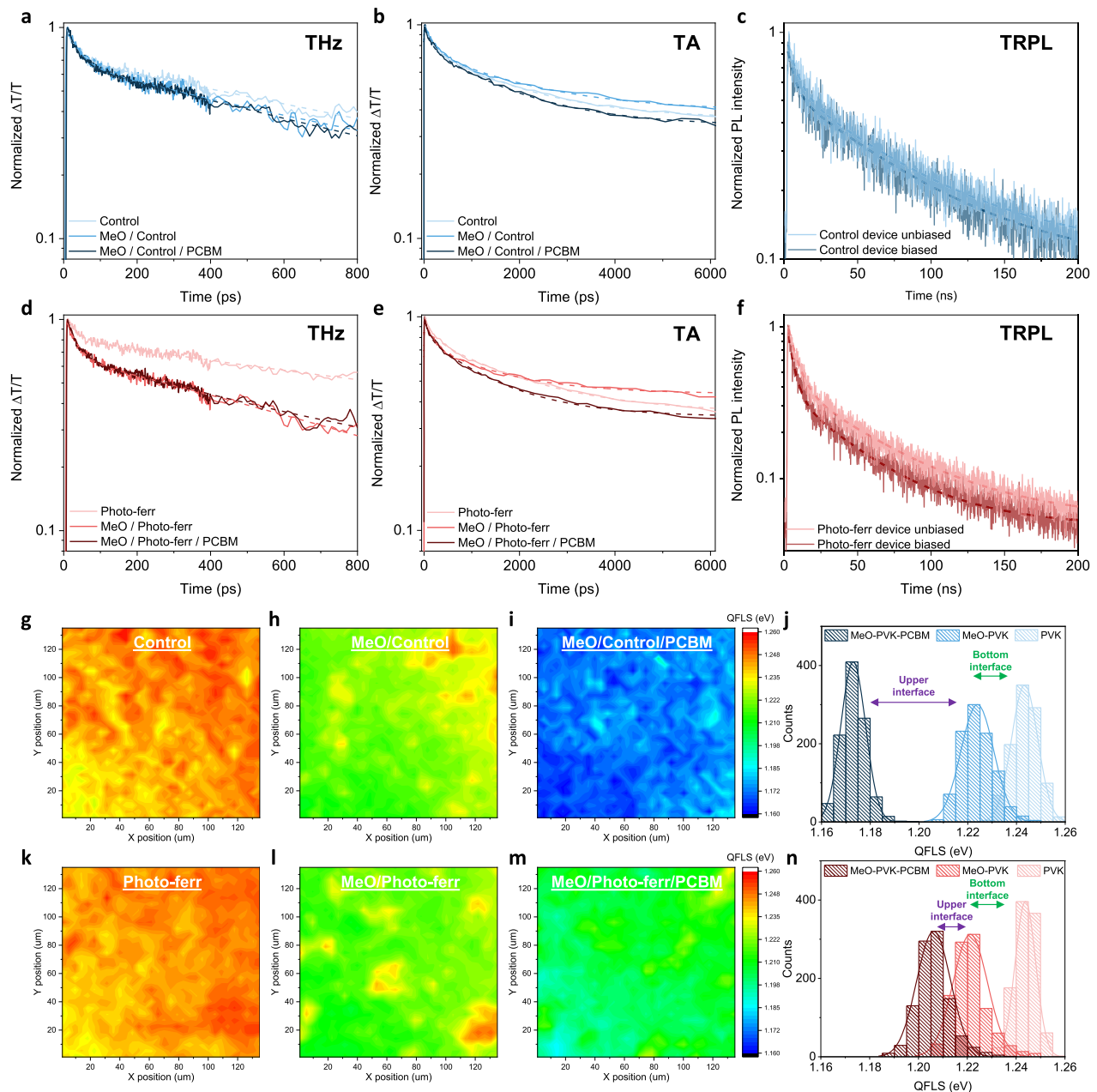
Fig. 4 | Steady-state and transient electro-optical analysis. Terahertz (THz), transient absorption (TA) and time resolved photoluminescence (TRPL) spectroscopy measurements (fitting traces in dashed lines) performed on different stacks configurations and with an initial charge carrier density of 10^{17} cm^{-3} for control (**a–c**) and photo-ferroelectric samples (**d–f**), respectively. Quasi-fermi level splitting (QFLS) maps extrapolated from PLQY images of neat perovskite layer (**g**, **k**), perovskite layer deposited upon MeO-2Pacz (**h**, **l**) and the full stack comprising MeO-2Pacz-perovskite-PCBM (**i**, **m**) for control and photo-ferroelectric samples, respectively. The maps represent the QFLS distribution on the surface of the layer in a range from 1.16 eV to 1.26 eV. QFLS histograms (**j**, **n**) extrapolated from the QFLS maps of the same device stacks reported in (**g–i**) and (**k–m**), respectively.

photoconductivity decay. Thus, it appears that a more efficient (increased inverse rate, τ_1) charge transfer[37–39] to the bottom layer of MeO-2PACz occurs, which acts as a hole extraction layer. This acceleration is a direct consequence of the photo-ferroelectric effect. To further confirm its impact, we performed time-resolved photoluminescence (TRPL) measurements under applied external bias (Fig. 4c, f, respectively). Under 1-sun equivalent excitation, a biexponential fit was used to parametrize the PL decay dynamics. As expected, the applied bias had no effect on the control. Conversely, in the case of the photo-ferroelectric-based device both lifetime components were affected by the external bias: τ_1 decreased (see Table 2), while τ_2 increased. This observation confirms the role of the

ferroelectric polarization in enhancing charge extraction by separating charges, improving hole transfer, and reducing the overall charge recombination. Additional analysis with back-side illumination revealed similar behavior, further validating these observations (Fig. S21).

To further explore the role of the photo-ferroelectric sandwich in limiting charge carrier recombination, we map the quasi Fermi level splitting (QFLS) determined from hyperspectral PL intensity mapping (calculated using Eq. S3)[34] for both the control and photo-ferroelectric stacks represented in Fig. 4g–i and Fig. 4k–m, respectively. The corresponding energy histograms are reported in Fig. 4j, n (see also Figs. S22 and S23). For both the control and photo-ferroelectric neat perovskite samples, the measured QFLS peaks at 1.245 eV, very close to

Table 1 | Terahertz (THz) and transient absorption (TA) lifetime analysis

	TeraHertz		Transient Absorption	
	τ_1 (ns)	τ_2 (ns)	τ_1 (ns)	τ_2 (ns)
Ctrl	28.7 ± 1.9	1120 ± 132	128.2 ± 8.3	1414 ± 65
MeO-Ctrl	29.3 ± 2.6	862 ± 108	129.5 ± 12.1	1265 ± 64
MeO-Ctrl-PCBM	29.4 ± 1.5	793 ± 121	127.1 ± 9.9	1224 ± 71
Ferr	28.2 ± 1.7	1150 ± 189	153.5 ± 8.2	1641 ± 92
MeO-Ferr	24.1 ± 1.1	1090 ± 142	93.4 ± 6.2	1402 ± 78
MeO-Ferr-PCBM	24.3 ± 1.1	1003 ± 135	92.9 ± 5.8	1523 ± 65

Lifetime components values are obtained from a bi-exponential fitting procedure on THz and TA data for control and photo-ferroelectric stacks.

Table 2 | Time resolved photoluminescence (TRPL) lifetime analysis

	Time resolved PL	
	τ_1 (ns)	τ_2 (ns)
Ctrl unbiased	8.0 ± 0.6	66.1 ± 8.9
Ctrl biased	7.8 ± 0.5	69.2 ± 7.2
Ferr unbiased	6.6 ± 0.4	68.4 ± 5.9
Ferr biased	4.5 ± 0.4	83.2 ± 6.1

Lifetime components values are obtained from a bi-exponential fitting procedure on TRPL data for both control and photo-ferroelectric devices with and without bias.

the radiative limit of 1.253 eV (Fig. 3g), indicating excellent bulk perovskite quality. Considering the MeO-2PACz/perovskite stacks, we observe a slight decrease in the QFLS, shifting to around 1.225 eV for both samples, due to the addition of the bottom interface. This similar behavior suggests that no additional recombination arises from the modified interface (despite the faster decay observed in the THz and TA signals). On the contrary, striking differences between the control and the photo-ferroelectric samples arise when considering the full device stack. The control sample experienced a severe QFLS quenching of 50 meV, while the photo-ferroelectric device only showed a decrease of 20 meV. This result further confirms the role of the interface in reducing non-radiative recombination pathways at the upper interface, leading to a QFLS of 1.206 eV for the complete stack – in good agreement with the measured V_{OC} value of 1.21 eV. Overall, the 2D-based photo-ferroelectric interfaces allow to address simultaneously both the bottom and upper interfaces by improving charge transfer at the HTL/perovskite side, while lowering the non-radiative recombination pathways at the perovskite/ETL one, ultimately boosting the device V_{OC}.

In conclusion, our work provides the experimental observation of a photo-ferroelectric 2D/3D/2D perovskite interface which we design, characterize and integrate in a working perovskite solar cell. As a result of the interface modification, the additional electrical field induced by spontaneous polarization in the ferroelectric 2D layer adds to the device built-in, driving interfacial charges apart and reducing their recombination. This observation stems true for different 3D perovskite band gaps, broadening the relevance of our approach.

The photo-ferroelectric interface boosts the device V_{OC} to 1.21 V resulting in the highest value reported for highly efficient (i.e., PCE > 22%) perovskite solar cells, serving as proof of concept for its fundamental validity. By analysing the photoinduced charge dynamics we reveal that the photo-ferroelectric interface plays a dual role: promoting interfacial charge separation and minimizing non-radiative recombination, thereby enhancing charge extraction. The experimental evidence is corroborated by first-principles simulations showing the formation of a coherent 2D/3D interface with a specific molecular orientation which positively modifies the interfacial electrostatic potential. This concept opens a new path for the advancement of perovskite materials and interface engineering by leveraging the electrostatic fields produced by polar building blocks, with immediate impact on the working mechanisms and performances of optoelectronic devices.

Methods

Materials

Solvents were purchased from Sigma-Aldrich (highest purity and anhydrous); PbI_2, $PbBr_2$, CsI (99.99% purity) and MeO-2PACz ([2-(3,6-Dimethoxy-9H-carbazol-9-yl)ethyl]phosphonic Acid) were purchased from TCI; organic halide salts were purchased from GreatCell Solar. 2-thiopheneethylammonium halide salts were synthesized following a previously reported protocol for TEA.HI[28] (6,6)-PhenylC61 butyric acid methyl ester (PCBM, >99.5%) and Bathocuproine (BCP, sublimed grade, 99.99% purity) were purchased from Lumtec. Unless otherwise specified, materials and solvents have been used as received. All the solutions were prepared into an Ar-filled glovebox and the spin coating steps were carried out into a N_2-filled glovebox (in both cases, O_2 and H_2O concentration were <0.1 ppm).

Synthesis of (4,4-DFPD)$_2$PbI$_4$ single crystals

Crystals of ((4,4-DFPD)$_2$PbI$_4$ were prepared by mixing stoichiometric amounts of PbI2 (2.3 g) and 4,4-difluoropiperidinium hydrochloride (1.58 g) in the HI solution (25 mL, 47 wt % in water) in a 500 mL round-bottomed flask. The orange precipitates that were produced were dissolved by heating to 443 K to get a clear solution. Slowly cooling the solution resulted in the formation of orange crystals of (4,4-DFPD)$_2$PbI$_4$. The orange precipitate was washed with toluene and collected under hirsch filtration.

Perovskite solar cell fabrication

Prepatterned ITO/glass substrates were sequentially cleaned with acetone and 2-propanol (IPA) by ultrasonication for 15 min in each solvent. The ITO/glass substrates were then dried with N_2 and treated with oxygen plasma at 100 mW for 10 min. The substrates were moved into the glovebox for subsequent layers deposition. The MeO-2PACz self-assembly monolayers were deposited by spin coating (3000 rpm, 30 s, 1500 rpm/s) from a 0.335 mg/mL solution in ethanol, and then annealed at 100 °C for 10 min. The perovskite precursor solution (1.2 M) was prepared with the mixed cations (Pb, Cs, FA and MA) and halides (I and Br) composition, dissolved in a solvent mixture (DMF:DMSO = 4:1 vol:vol) according to the formula $Cs_{0.05}FA_{0.79}MA_{0.16}Pb(I_{0.90}Br_{0.10})_3$ with an excess of PbI_2 of 5%. For the ferroelectric samples, we synthetize the (4,4-DFPD)$_2$PbI$_4$ perovskite single crystals and, by dissolving them in a solution DMF:DMSO 4:1, we incorporate it into the 3D perovskite solution with different molar ratios (0.05, 0.03, 0.015 mol% with respect to halogen atom). The perovskite layer was deposited via a two-step spin-coating procedure at 1000 and 5000 rpm for 12 and 27 s, respectively. Chlorobenzene antisolvent was dripped on the spinning substrate 7 s before the end of the spin coating program. Subsequently, the samples were annealed at 100 °C for 30 min. Then, TEACl solution (1.5 mg/mL in IPA) were spin coated dynamically onto the perovskite substrates with a single step program (5000 rpm, 25 s, 2500 rpm/s). Subsequently, the substrates were dried at 100 °C for 5 min. For all the samples, the PCBM solution (20 mg/mL in chlorobenzene) was spin coated dynamically with a single step program (2000 rpm, 30 s, 1000 rpm/s), followed by 10 min annealing at 100 °C. Lastly, the thin layers of BCP (0.5 mg/mL in IPA), were spin coated at 4000 rpm for 30 s, with a ramping rate 1000 rpm/s. The devices were then completed by depositing 80 nm-thick silver (Ag) back electrode through thermal evaporation.

Photovoltaic device characterization

Current density voltage measurements were performed in ambient conditions under simulated AM1.5 light with an intensity of

100 mW cm^{-2} (Wavelabs-Sinus 70). The intensity was calibrated using a Si reference cell. Cells were scanned using a Keithley 2450 source-meter forward and reverse from −0.3 V to 1.23 V, with a scanning velocity of 100 mV/s. The pixel area was 3.2 mm by 1.5 mm, corresponding to the overlapping region among ITO and top metal contact. JV characterizations are performed adopting a solar cell mask with aperture 0.03 cm^2. The external quantum efficiency (EQE) measurements were performed using ARKEO platform (Cicci Research S.r.l.). The light from a chopped halogen lamp is shone on the device and the response is compared with a calibrated reference cell, through an automated routine. The software provides the IPCE spectrum.

Time of Flight - Secondary Ion Mass Spectroscopy (ToF-SIMS) measurements

ToF-SIMS analyses were performed using a ToF-SIMS 5-100 instrument, with the pulsed primary ions from a Bi^{3+} (30 keV) liquid−metal ion gun for sputtering and a MCs$^+$ pulsed primary ion beam for analysis (30 keV), the detection area was $150 \times 150\,\mu$m.

Transmission Electron Microscopy (TEM) measurements and focused ion beam (FIB)

For the cross-sectional Transmission Electron Microscopy (TEM)-based study, an electron-transparent lamella was prepared using a focused ion beam (FIB) equipped scanning electron microscope (SEM-FIB Helios G5 DualBeam, FEI) with the assistance of an EasyLift nano-manipulator and a Gallium (Ga) ion source. To protect the region of interest during FIB processing, two types of protective coatings were deposited: first, a 0.5 μm layer of W coating applied using the e-beam, followed by a 3 μm layer of W coating deposited by the ion beam for final protection. The ion beam milling procedure was carried out step by step, with a beam current of 2.4 nA, 0.44 nA, 0.26 nA, 0.045 nA, and 0.025 nA, gradually reducing it from 30 kV to 5 kV, in order to cut and thin down the lamella to 60 nm while minimizing ion beam damage. Additionally, a low current cleaning process (5-2 kV, 81-28 pA) was performed to eliminate potential contamination. TEM-based experiments were conducted in both parallel beam mode high-resolution TEM (HR-TEM) and converge beam scanning TEM (STEM) mode using a Double Cs corrected ThermoFisher™ Themis 60−300 Cubed TEM microscope operating at 80 kV. TEM data processing was carried out using Gatan™ Digital Micrograph and the Thermo Scientific™ Velox suites.

Atomic force microscopy (AFM) and Piezo-response Force Microscopy (PFM) measurements.

AFM and PFM measurements were performed with a TriA-SPM microscope (A.P.E. Research S.r.l., Trieste, Italy) in contact mode, using NSC15/Al:BS probes (Mikromasch − Innovative Solutions Bulgaria Ltd.) on a scanning an area of $5 \times 5\,\mu$m and applying an external bias of +3 V and −3 V. AFM and PFM images were edited with Gwyddion software, which allows to retrieve signal profiles at specific regions of the samples.

Photoluminescence (PL), Transient Photoluminescence (TRPL), Hyperspectral mapping, UV-VIS Absorption measurements

PL and TRPL measurements were performed on a custom-made setup[40]. Laser excitation was provided by a pulsed 470 nm laser (PicoQuant, LDH-DC-470) with 30 um spot diameter. Both PL spectra and TRPL decays are obtained from horizontal and vertical cuts of a 2D time-wavelength map acquired with a 1 Sun equivalent excitation and 2.5 MHz repetition rate.

The Hyperspectral photoluminescence imaging was performed using a hyperspectral microscope (Photon etc). The laser excitation at 405 nm was focused on the sample through a microscope objective 20×. The excitation intensity was adjusted to ~1 Sun by illuminating a contacted perovskite solar cell (short circuit) and matching the current density to the short-circuit current measured in the J−V sun simulator.

1-sun equivalent condition is obtained by shining laser light on a perovskite solar cell used as a reference. By tuning the laser intensity in order to match the short circuit current density measured under the solar simulator illumination, ensure the 1-sun condition.

The UV-VIS absorption spectra of the perovskite thin films were collected using a commercial UV−NIR spectrophotometer (Lambda1050 + , Perkin Elmer) in the range 350−950 nm with 1 nm/s scan speed.

Transient Photovoltage (TPV), Time − Resolved Terahertz (TRTS) and Femtosecond Transient Absorption (TA) measurements

TPV analyses were performed in ambient air conditions with a Cicci Research Arkeo transient tests module. Measurements were conducted under constant 1 sun illumination and the constant bias was perturbed with short light pulses of 200 μs width.

TRTS was conducted using a home-built optical pump − THz probe setup[41]. The output of a Ti:sapphire regenerative amplifier (Coherent LEGEND DUO, 800 nm, 4.5 mJ, 3 kHz, 100 fs) was used as the laser source and was split into four beam: three beams were used to pump optical parametric amplifiers (OPA; Light Conversion TOPAS Prime) with pulse energies of 2 mJ, 1 mJ, and 1 mJ; and the fourth beam (0.5 mJ) remained unconverted. A fraction (360 μJ) of the fundamental output of the Ti:sapphire amplifier was split into 2 additional paths: one for THz generation, and the other for a time-delayed gating beam. The generation beam was directed through a 1 mm thick <100 >-oriented ZnTe crystal, whereby optical rectification produced sub-picosecond, single-cycle THz pulses as the probe. The THz probe transmission (T) was measured via electrooptic sampling (EOS) in a second 1 mm thick ZnTe crystal with the delay-adjustable gating pulse. EOS detection was achieved using a balanced photodetector (New Focus, 2107) connected to a lock-in amplifier (SR830, Stanford Research Systems). The 2 mJ-pumped TOPAS generated wavelength-tuneable pump pulses (using Light Conversion NIRUVIS extension). The pump was fixed at 470 nm with a fluence of 189 μJ/cm^2 and was delayed relative to the probe using a mechanical delay stage (Thorlabs DDS300/M), generating delays from −100 ps to 4 ns. All the THz-related optics were placed in a closed chamber, continuously purged with pure nitrogen gas. THz probe pulses and optical pump pulses were chopped at 1497 Hz and 499 Hz by two optical choppers, respectively, to collect dark and excited state signals with one lock-in amplifier by adjusting its harmonic reference.

To measure the frequency-dependent complex photo-conductivity and THz absorption spectra, the pump pulse was fixed at a delay time of 14 ps after photoexcitation, and the gating pulse was scanned to obtain the pump-induced change in transmission (ΔT) of the THz waveform in the time-domain. The complex photo-conductivity ($\Delta\sigma$) of the film was calculated using the thin-film approximation[42]:

$$\Delta\sigma = -\varepsilon_0 c (n_a + n_b)\frac{\Delta T}{T}$$

where n_a and n_b were the refractive indices of the surrounding material and the substrate, respectively (1.0 and 2.13 for N$_2$ and z-cut quartz substrate, respectively), and ε_0 and c were the permittivity of free space and the speed of light in vacuum, respectively. The effective charge carrier mobility was then calculated by:

$$\mu = \frac{\Delta\sigma A_{\text{eff}}}{qN}$$

where A_{eff} was the effective area of the overlap of optical pump and THz probe pulses, q was the elementary charge, and N was the absorbed carrier density.

Femtosecond TA spectroscopy was carried out using a home-built pump-probe setup, using the same Ti:sapphire amplifier as was used for TRTS experiments. One of the 1 mJ-pumped TOPAS's was used to generate wavelength-tunable pump pulses (240–2600 nm, using Light Conversion NIRUVIS extension), which was fixed at 470 nm with a fluence of 65 μJ/cm^2. The final 1 mJ-pumped TOPAS was used to generate signal and idler only (1160–2600 nm), which was fixed to 1300 nm and was used as the seed for white light generation by focusing a portion of it through a continuously moving CaF$_2$ crystal, thereby generating a white light supercontinuum from 350 nm to 1100 nm. The pump-probe delay time was achieved by varying the probe path length using a broadband retroreflector mounted on a 600 mm automated mechanical delay stage (Thorlabs optical delay line ODL600/M), generating delays from −0.5 ns to 7.5 ns.

Pump and probe beams were focused onto the film-side of the sample to spot sizes of 0.84 mm and 0.09 mm average diameter (from a Gaussian fit at 86.5% intensity), as measured using a beam profiler (Coherent LaserCam-HR II). The transmitted fraction of the white light probe was guided to a custom-made prism spectrograph (Entwicklungsbüro Stresing) where it was dispersed by a prism onto a 512-pixel NMOS linear image sensor (Hamamatsu S8381-512Q). The probe pulse repetition rate was 3 kHz, while the excitation pulses were mechanically chopped to 1.5 kHz, and the detector array was read out at 3 kHz. Adjacent diode readings corresponding to the transmission of the sample after excitation and in the absence of an excitation pulse were used to calculate ΔT/T. Measurements were averaged over several thousand shots to obtain a good signal-to-noise ratio. The chirp induced by the transmissive optics was corrected with a home-built Matlab code.

X-Ray Photoemission Spectroscopy (XPS) and Ultraviolet Photoemission Spectroscopy (UPS) measurements

XPS measurements were carried out through a Kratos Axis UltraDLD spectrometer (Kratos Analytical Ltd.) with a mono-chromated Al KαX-ray source (hν = 1486.6 eV) operating at 20 mA and 15 kV. Each sample was ground to the sample holder via copper tape to maximize its electrical conductivity. The wide scans were collected over an analysis area of 300×700 μm^2 at a photoelectron pass energy of 160 eV and energy step of 1 eV, while high-resolution spectra were collected at a photoelectron pass energy of 10 eV and an energy step of 0.1 eV. A take-off angle of 0° with respect to sample normal direction was used for all analyses. The spectra were referenced to the adventitious carbon 1 s peak at 284.8 eV. The spectra were analysed with the Casa XPS software (Casa Software Ltd., version 2.3.24).

Scanning Electron Microscopy measurements

Scanning electron microscopy (SEM) images were taken at 3 kV accelerating voltage with 30 μm 88 beam aperture, using a Zeiss Auriga microscope equipped with an in-lens detector.

Interfacial modeling details

Models of the interface between (4,4-DFPD)$_2$PbI$_4$ and FAPbI$_3$ were constructed along [001] using averaged in-plane lattice constants from the separate bulk materials. The charge density difference (CDD) and local potential difference (LPD) for the fully relaxed antiferroelectric interface configuration were computed following equations:

$$CDD = \rho_{antiferro}^{intf} - \rho_{antiferro}^{LDP} - \rho_{antiferro}^{3D}$$

$$LPD = \phi_{antiferro}^{intf} - \phi_{antiferro}^{LDP} - \phi_{antiferro}^{3D}$$

where $\rho_{antiferro}^{intf}, \rho_{antiferro}^{LDP}$, and $\rho_{antiferro}^{3D}$ are the charge density of the antiferroelectric 2D/3D interface supercell, 2D slab model and 3D slab model, respectively. $\phi_{antiferro}^{intf}, \phi_{antiferro}^{LDP}$, and $\phi_{antiferro}^{3D}$ stand for the

local potentials. Then, LPD induced by molecular reorientation for ferroelectric interface configurations were calculated from:

$$LPD = \phi_{ferro}^{intf} - \phi_{antiferro}^{intf}$$

where ϕ_{ferro}^{intf} is the local potential of the ferroelectric 2D/3D interface supercells. We note that to isolate the impact of interfacial molecular dipole on the potential difference, no ionic relaxation was performed for ferroelectric interface configurations (i.e., only the orientation of 4,4-DFPD at the interface are altered).

The underlying calculations were performed based on the Kohn–Sham density functional theory (DFT)[43] as implemented in the Vienna Ab Initio Simulation Package (VASP)[44,45]. Projector augmented-wave (PAW)[46,47] pseudopotentials were used to treat core atomic states, and the valence electron configuration of H, C, N, F, Pb, and I are treated explicitly by 1($1s^1$), 4($2s^2 2p^2$), 5($2s^2 2p^3$), 7($2s^2 2p^5$), 14($5d^{10} 6s^2 6p^2$), 7($5s^2 5p^5$), respectively. The Perdew–Burke–Ernzerhof exchange-correlation functional (PBE)[48] with the Grimme D3[49] scheme for vdW corrections (i.e., PBE + D3) were employed. The plane-wave kinetic energy cutoff of 700 eV and a $4 \times 4 \times 1$ Γ-centered k-mesh were adopted during all calculations. The convergence criteria were set to 10^{-6} eV and 5×10^{-2} eV Å^{-1} for total energy and atomic forces, respectively.

Grazing incidence wide angle X-ray scattering

GIWAXS reciprocal maps were measured with a custom-made laboratory system comprising a MetalJet X-ray source (Excillum) with an X-ray energy of 9.25 keV (λ = 1.34 Å). All the samples were measured in a vacuum to suppress the scattering from the air. The air scattering would increase the signal-to-noise ratio for the diffractions in the vicinity of the direct and reflected X-ray beam (i.e., diffraction pattern originating from the 2D perovskite structures).

Reporting summary

Further information on research design is available in the Nature Portfolio Reporting Summary linked to this article.

Data availability

The data produced and analysed during the current study are available from the first author (G.P) and the corresponding author (G.G) upon request.

References

1. Cheng, Y. & Ding, L. Pushing commercialization of perovskite solar cells by improving their intrinsic stability. *Energy Environ. Sci.* **14**, 3233–3255 (2021).
2. Li, B. & Zhang, W. Improving the stability of inverted perovskite solar cells towards commercialization. *Commun. Mater.* **3**, 1–13 (2022).
3. Zhu, P. et al. Toward the Commercialization of Perovskite Solar Modules. *Adv Mater*. **36**, 2307357 (2024).
4. Li, Z. et al. Stabilized hole-selective layer for high-performance inverted p-i-n perovskite solar cells. *Science* **382**, 284–289 (2023).
5. Park, S. M. et al. Low-loss contacts on textured substrates for inverted perovskite solar cells. *Nature* **624**, 289–294 (2023).
6. Liang, Z. et al. Homogenizing out-of-plane cation composition in perovskite solar cells. *Nature* **624**, 557–563 (2023).
7. Ji, R. et al. Perovskite phase heterojunction solar cells. *Nat. Energy* **7**, 1170–1179 (2022).
8. Jang, Y.-W. et al. Intact 2D/3D halide junction perovskite solar cells via solid-phase in-plane growth. *Nat. Energy* **6**, 63–71 (2021).
9. Sutanto, A. A. et al. 2D/3D perovskite engineering eliminates interfacial recombination losses in hybrid perovskite solar cells. *Chem* **7**, 1903–1916 (2021).
10. Azmi, R. et al. Double-side 2-dimensional/3-dimensional heterojunctions for inverted perovskite solar cells. *Nature* **628**, 93–98 (2024).

11. Wu, M. 100 years of ferroelectricity. *Nat. Rev. Phys.* **3**, 726–726 (2021).
12. Fernandez, A. et al. Thin-film ferroelectrics. *Adv. Mater.* **34**, 2108841 (2022).
13. Kreisel, J., Alexe, M. & Thomas, P. A. A photoferroelectric material is more than the sum of its parts. *Nat. Mater.* **11**, 260–260 (2012).
14. Butler, K. T., Frost, J. M. & Walsh, A. Ferroelectric materials for solar energy conversion: photoferroics revisited. *Energy Environ. Sci.* **8**, 838–848 (2015).
15. Manzi, M. et al. Ferroelectricity in hybrid perovskites. *J. Phys. Chem. Lett.* **14**, 3535–3552 (2023).
16. Paillard, C. et al. Photovoltaics with ferroelectrics: current status and beyond. *Adv. Mater.* **28**, 5153–5168 (2016).
17. Schulz, A. D. et al. On the ferroelectricity of CH3NH3PbI3 perovskites. *Nat. Mater.* **18**, 1050–1050 (2019).
18. Röhm, H., Leonhard, T., Hoffmann, M. J. & Colsmann, A. Ferroelectric domains in methylammonium lead iodide perovskite thin-films. *Energy Environ. Sci.* **10**, 950–955 (2017).
19. Röhm, H., Leonhard, T., Hoffmann, M. J. & Colsmann, A. Ferroelectric poling of methylammonium lead iodide thin films. *Adv. Funct. Mater.* **30**, 1908657 (2020)
20. Zhang, Y. et al. Ferroelectricity in a semiconducting all-inorganic halide perovskite. *Sci. Adv.* **8**, eabj5881 (2022).
21. Sharada, G. et al. Is CH3NH3PbI3 polar? *J. Phys. Chem. Lett.* **7**, 2412–2419 (2016).
22. Eames, C. et al. Ionic transport in hybrid lead iodide perovskite solar cells. *Nat. Commun.* **6**, 7497 (2015).
23. Frost, J. M., Butler, K. T. & Walsh, A. Molecular ferroelectric contributions to anomalous hysteresis in hybrid perovskite solar cells. *APL Mater.* **2**, 081506 (2014).
24. Li, Z. et al. Efficient charge transport in inverted perovskite solar cells via 2D/3D ferroelectric heterojunction. *Small Methods* 2400425 https://doi.org/10.1002/smtd.202400425 (2024).
25. Chen, W. et al. High-polarizability organic ferroelectric materials doping for enhancing the built-in electric field of perovskite solar cells realizing efficiency over 24%. *Adv. Mater.* **34**, 2110482 (2022).
26. Ollearo, R. Multidimensional perovskites for high detectivity photodiodes. *Adv. Mater.* **34**, e2205261 (2022).
27. Cho, K. T. et al. Water-repellent low-dimensional fluorous perovskite as interfacial coating for 20% efficient solar cells. *Nano Lett.* **18**, 5467–5474 (2018).
28. Zhang, H.-Y. et al. Observation of vortex domains in a two-dimensional lead iodide perovskite ferroelectric. *J. Am. Chem. Soc.* **142**, 4925–4931 (2020).
29. Zanetta, A. et al. Manipulating color emission in 2D hybrid perovskites by fine tuning halide segregation: a transparent green emitter. *Adv. Mater.* **34**, e210594 (2022).
30. Xing, J. et al. Color-stable highly luminescent sky-blue perovskite light-emitting diodes. *Nat. Commun.* **9**, 3541 (2018).
31. Röhm, H. et al. Ferroelectric properties of perovskite thin films and their implications for solar energy conversion. *Adv. Mater.* **31**, 1806661 (2019).
32. Zhong, Y. Inhibition of ion migration for highly efficient and stable perovskite solar cells. *Adv. Mater.* **35**, e2302552 (2023).
33. Stolterfoht, M. et al. The impact of energy alignment and interfacial recombination on the internal and external open-circuit voltage of perovskite solar cells. *Energy Environ. Sci.* **12**, 2778–2788 (2019).
34. Stolterfoht, M. et al. Visualization and suppression of interfacial recombination for high-efficiency large-area pin perovskite solar cells. *Nat. Energy* **3**, 847–854 (2018).
35. Peng, W. et al. Reducing nonradiative recombination in perovskite solar cells with a porous insulator contact. *Science* **379**, 683–690 (2023).
36. Abdi-Jalebi, M. et al. Charge extraction via graded doping of hole transport layers gives highly luminescent and stable metal halide perovskite devices. *Sci. Adv.* **5**, eaav2012 (2019).
37. Marchioro, A. et al. Unravelling the mechanism of photoinduced charge transfer processes in lead iodide perovskite solar cells. *Nat. Photonics* **8**, 250–255 (2014).
38. Serpetzoglou, E. et al. Improved carrier transport in perovskite solar cells probed by femtosecond transient absorption spectroscopy. *ACS Appl. Mater. Interfaces* **9**, 43910–43919 (2017).
39. Brauer, J. C., Lee, Y. H., Nazeeruddin, M. K. & Banerji, N. Charge transfer dynamics from organometal halide perovskite to polymeric hole transport materials in hybrid solar cells. *J. Phys. Chem. Lett.* **6**, 3675–3681 (2015).
40. Pica, G., Bajoni, D. & Grancini, G. A step beyond in steady-state and time-resolved electro-optical spectroscopy: Demonstration of a customized simple, compact, low-cost, fiber-based interferometer system. *Struct. Dyn.* **9**, 011101 (2022).
41. Wang, M. et al. Photo-induced enhancement of lattice fluctuations in metal-halide perovskites. *Nat. Commun.* **13**, 1019 (2022).
42. Milot, R. L., Eperon, G. E., Snaith, H. J., Johnston, M. B. & Herz, L. M. Temperature-dependent charge-carrier dynamics in CH3NH3PbI3 perovskite thin films. *Adv. Funct. Mater.* **25**, 6218–6227 (2015).
43. Kohn, W. & Sham, L. J. Self-consistent equations including exchange and correlation effects. *Phys. Rev.* **140**, A1133–A1138 (1965).
44. Kresse, G. & Furthmüller, J. Efficient iterative schemes for ab initio total-energy calculations using a plane-wave basis set. *Phys. Rev. B* **54**, 11169–11186 (1996).
45. Kresse, G. & Furthmüller, J. Efficiency of ab-initio total energy calculations for metals and semiconductors using a plane-wave basis set. *Comput. Mater. Sci.* **6**, 15–50 (1996).
46. Kresse, G. & Joubert, D. From ultrasoft pseudopotentials to the projector augmented-wave method. *Phys. Rev. B* **59**, 1758–1775 (1999).
47. Blöchl, P. E. Projector augmented-wave method. *Phys. Rev. B* **50**, 17953–17979 (1994).
48. Perdew, J. P., Burke, K. & Ernzerhof, M. Generalized gradient approximation made simple. *Phys. Rev. Lett.* **77**, 3865–3868 (1996).
49. Grimme, S., Antony, J., Ehrlich, S. & Krieg, H. A consistent and accurate ab initio parametrization of density functional dispersion correction (DFT-D) for the 94 elements H-Pu. *J. Chem. Phys.* **132**, 154104 (2010).

Acknowledgements

Author contributions

G.P. developed the whole work, coordinating experiments and being responsible of all the experimental part described in the paper. L.P. synthetized the 2D single crystals; C.E.P. and F.L. supervised THz and TA

spectroscopy measurements; B.V. conducted TEM measurements and analysis under the supervision of S.D.W.; F.T. encapsulated the devices; C.D. performed the ToF-SIMS measurements under the supervision of C.-Q. M.; Y.-K. J. conducted theoretical calculations under the supervision of A.W.; M.P. performed the UPS and XPS measurements and analysis; N.M. and P.S. performed GIWAXS measurements and analysis. G.P., G.G., and A.W. wrote the manuscript. All the authors contributed to reviewing the manuscript. G.G. supervised the overall project and directed the research. All authors contributed to the manuscript.

Competing interests

The authors declare no competing interests.

Additional information

Supplementary information The online version contains supplementary material available at
https://doi.org/10.1038/s41467-024-53121-8.

Correspondence and requests for materials should be addressed to Giulia Grancini.

Peer review information *Nature Communications* thanks the anonymous reviewer(s) for their contribution to the peer review of this work. A peer review file is available.

Publisher's note Springer Nature remains neutral with regard to jurisdictional claims in published maps and institutional affiliations.